




PAPER

[View Article Online](#)
[View Journal](#)

Cite this: DOI: 10.1039/d3ta07591e

An electrolyte additive of bromoxoindole enables uniform Li-ion flux and tunable Li₂S deposition for high-performance lithium–sulfur batteries†Jinxuan Zou,^a Pengxuan He,^a Yufang Zhang,^a Dong Cai,^a ^{*,a} Shuo Yang,^{*,b} Ying He,^a Yangyang Dong,^a Kuikui Xiao,^a Xuemei Zhou,^a ^a Huagui Nie^a and Zhi Yang ^{*,a}

Low discharge capacity and rapid capacity decay are the main causes that hinder the commercialization of lithium–sulfur (Li–S) batteries. A feasible strategy is to modify electrolytes which aims at accelerating sulfur conversion reactions and restraining side reactions on both electrodes. However, simultaneously increasing the reactivity of sulfur and reducing the reactivity of Li poses great challenges. Herein, an electrolyte additive of 6-bromoxoindole (BOD) was introduced into Li–S batteries. Through a systematic study, it is found that the BOD can dissolve in electrolytes, undergo partial deprotonation, and react with LiTFSI/LiPSs to form BOD–Li–TFSI/BOD–Li–PS solvation structures. The Li⁺ transfer kinetics and sulfur conversion reactions were significantly enhanced with 0.5 wt% BOD addition, and meanwhile, the Li anode maintained stable plating/stripping behavior. As a result, the cell delivered a high discharge capacity of 811 mA h g^{−1} at a sulfur loading of 5 mg cm^{−2} and E/S ratio of 8 μL mg^{−1} at ambient temperature and could also work stably at a low temperature of −20 °C.

Received 8th December 2023

Accepted 24th January 2024

DOI: 10.1039/d3ta07591e

rsc.li/materials-a

Introduction

The lithium–sulfur (Li–S) battery is considered to be a promising high-energy storage system owing to its ultra-high theoretical energy density (2600 W h kg^{−1}), cost-effectiveness, and abundant reserves of its constituent materials.^{1–3} However, commercial Li–S batteries still face many challenges, including the lithium polysulfide (LiPS) intermediate shuttle effect,⁴ poor sulfur conductivity on the cathode side,⁵ parasitic reactions,⁶ and safety hazards associated with Li dendrites on the anode side,^{7,8} all of which contribute to unstable cycling performance. Although there has been great progress in regulating the sulfur host,^{9,10} LiPS catalyst,¹¹ and Li anode interface layer,¹² improvements to individual electrodes may not address all the above issues.

The Li–S electrolyte is mainly used to conduct Li⁺ and maintain the voltage balance, bridging the sulfur cathode and Li anode.^{13–15} It causes interfacial side reactions at both electrodes, which largely determine the Li–S battery performance.^{16,17} Commonly used electrolytes for Li–S battery systems are prepared in a 1 : 1 volume ratio of 1,3-dioxolane (DOL) and 1,2-dimethoxyethane (DME), which allows the electrolyte to

have both low viscosity and high solubility for LiPSs, thus delivering high sulfur utilization.¹⁸ To further enhance Li⁺ transport and suppress the LiPS electromigration rate, Li salts such as lithium bis(trifluoromethanesulfonyl)imide (LiTFSI), lithium bis(fluorosulfonyl)imide (LiFSI), and lithium bis(oxalato)borate (LiBOB) are typically used as additives in the electrolyte.^{19,20}

Unfortunately, the above-mentioned Li salts are poorly soluble, which contributes to the issues affecting electrolytes and electrodes in this system. To address this problem, additives with appropriate functionality are used in commercially purchased batteries. In typical cases, P-containing additives have been proposed as flame retardants; F and cyanide groups (–CN) are used as high voltage additives; and Br/F-containing groups decompose to form a highly stable solid-state electrolyte interface (SEI).²¹ Nevertheless, efficient, low-cost, and multi-functional additives to improve Li–S battery performance are still required.

In recent work, Ai *et al.*²² achieved stable cycling performances on thick sulfur electrodes with the use of an *in situ* nucleophilic reaction of vinyl carbonate (VC) with LiPSs in ether-based electrolytes. This approach formed an intact CEI layer on the cathode surface and promoted direct conversion of S and Li₂S without any intermediate formation. Such a strategy may spur progress towards organic additives with adjustable functional groups that can regulate sulfur deposition at the cathode, enhance Li⁺ transport in electrolytes, and stabilize the Li anode under successive deposition and stripping cycles. In our previous work,^{23–25} we used biomimetic enzyme catalysts

^aKey Laboratory of Carbon Materials of Zhejiang Province, Wenzhou University, Wenzhou 325035, China. E-mail: caidong@wzu.edu.cn

^bCollege of Electrical and Electronic Engineering, Wenzhou University, Wenzhou 325035, China. E-mail: yangshuo@wzu.edu.cn

† Electronic supplementary information (ESI) available: Experimental section, and supplementary figures. See DOI: <https://doi.org/10.1039/d3ta07591e>

based on metal porphyrins or metal phthalocyanines with pyrrole rings in their skeleton, which showed excellent electron and hole transport properties. Indole, also referred to as benzopyrrole containing a pyrrole ring, and its derivative compounds are low in cost and electron-rich, and can be functionalized at a variety of grafting sites. Notably, the $-NH$ group of indole tends to undergo single electron oxidation reactions.^{26–28} This leads to alkali metal ions (such as Li^+ and Na^+) replacing H and binding to the N site, thereby forming organic–inorganic salts.^{29,30} This Li organic–inorganic salt formation regulates Li^+ transport^{31,32} and LiPS conversion characteristics. Additionally, the benzene ring group can easily be functionalized with different types and quantities of halogen atoms, which may be replaced by Li in ether-based electrolytes.³³ This behavior may regulate the solvation environment and promote uniform Li deposition. Hence, indole molecules and/or their derivatives are expected to synergistically regulate bulk electrolytes and their interfaces with both electrodes, to achieve high-performance Li–S batteries.

In this study, we investigated the effects of incorporating the additive 6-bromoxindole (BOD), which is composed of an amide-bonded pyrrole and a bromobenzene ring, into the standard Li–S electrolyte. By studying the Li_2S and Li deposition behaviors, Li^+ migration number, *in situ* spectra, and electrochemical performances, we found that BOD can dissolve in ether-based electrolytes, undergo partial deprotonation, and react with LiTFSI/LiPS to form BOD-Li-TFSI and/or BOD-Li-PS solvation structures. The Li transfer measured by the average Li^+ migration number was significantly enhanced and the Li_2S deposition mode changed from 2DP to 2DI, 3DP, and 3DI as the BOD concentration was increased from 0 to 5%. Furthermore, the Li anode maintained uniform Li-ion flux with the addition of 0.5% BOD. As a result, the 0.5% BOD cell delivered a high discharge capacity of 811 mA h g^{-1} at a sulfur loading of 5 mg cm^{-2} and E/S ratio of $8\text{ }\mu\text{L mg}^{-1}$ at ambient temperature and also operated stably at a low temperature of $-20\text{ }^\circ\text{C}$.

Experimental

Preparation of BOD electrolyte

Different weight ratios of BOD (0.1, 0.5, and 1 wt%) were directly added into standard Li–S electrolyte. This procedure was carried out in an argon-filled glove box with water and oxygen content below 0.1 ppm.

Preparation of the sulfur/carbon cathode (CNTs-S)

To synthesize the CNTs-S composite, the traditional co-melting method was used. The process involved mixing sulfur powder and carbon nanotubes in a mass ratio of 8 : 2. The sulfur content of the CNTs-S composites was kept at around 80 wt%. Subsequently, the slurry was prepared by uniformly dispersing 70 wt% CNTs-S powder, 10 wt% polyvinylidene fluoride (PVDF) binder, and 20 wt% CNT conductive additive in *N*-methyl pyrrolidone (NMP) solution. The slurry was stirred for 2 hours and then coated on aluminum foil. The coated foil was then evaporated at $55\text{ }^\circ\text{C}$ in a vacuum oven for 8 h. The resulting film was cut into

disks with a diameter of 12 mm. Unless otherwise stated, the sulfur loading on cathodes was approximately 1.2 mg cm^{-2} .

Cell assembly

A CR2025 coin cell was fabricated in an argon-filled glove box with water and oxygen content below 0.1 ppm. $40\text{ }\mu\text{L}$ electrolyte with the BOD additive was added to the separator between the CNTs-S cathode and Li sheet. Unless noted, the E/S ratio was controlled to be $\sim 20\text{ }\mu\text{L mg}^{-1}$ for the battery with a sulfur loading of 1.2 mg cm^{-2} , and $8\text{ }\mu\text{L mg}^{-1}$ for 5.0 mg cm^{-2} . The cell would reach equilibrium after resting for 8 hours.

Electrochemical measurements

Cyclic voltammetry (CV) measurements were performed on an electrochemical workstation (CHI 760E) in the voltage range of 1.6–2.8 V (vs. Li/Li^+). Electrochemical impedance spectroscopy (EIS) was performed in the frequency range of 100 kHz to 0.01 Hz at open-circuit voltage with an AC amplitude of 5 mV. For the assembly of the $Li||Li$ symmetric battery, two pieces of Li foil were used and $30\text{ }\mu\text{L}$ 0.5 wt% BOD electrolyte was added. Galvanostatic charge/discharge and $Li||Li$ symmetric tests were conducted on a Neware battery test system (Shenzhen Netware, China). The low-temperature test was conducted in a low-temperature refrigerator, and all batteries were placed in the refrigerator at least 8 hours before starting the test.

Material characterization

The microstructures of CNTs-S composites and electrodes after cycling were characterized using a scanning electron microscope (SEM, JSM-6700F). The Li anode for the symmetric batteries with each type of electrolyte was first cycled at 1 mA cm^{-2} and 1 mA h cm^{-2} for 200 cycles, then disassembled and rinsed with DME solution before SEM. Raman spectra were obtained on a Renishaw-inVia spectrometer with an argon ion laser (532 nm). FTIR spectra were recorded on a Nicolet iS 50 spectrometer (ThermoFisher Scientific, USA). Ultraviolet and visible (UV-vis) spectrophotometry was performed using a Shimadzu 1800 spectrometer in the range between 200 and 1100 cm^{-1} to characterize the polysulfide species in the cell. Surface elemental analysis was performed on an X-ray photoelectron spectrometer (PHI (China) Limited).

Results & discussion

Reversible BOD evolution in Li–S chemistry

To confirm the reactivity of the BOD additive, we first tested its reaction with LiPSs. Fig. 1a shows photographs of standard ether-based electrolyte (DOL/DME, v/v = 1 : 1) with 2 mM of Li_2S and Li_2S_6 , before and after the addition of BOD, where the color changed from pink to dark red as the Li_2S gradually dissolved in the modified electrolyte. The Li_2S dissolution and accompanying color change indicated that BOD was strongly polarizing and changed the solvation environments of Li_2S and LiPSs (Fig. S1†). Ultraviolet-visible (UV-vis) spectroscopy was performed to examine the structural transformations (Fig. 1b, S2 and S3†). A new peak emerged at $\sim 551\text{ nm}$, which was assigned

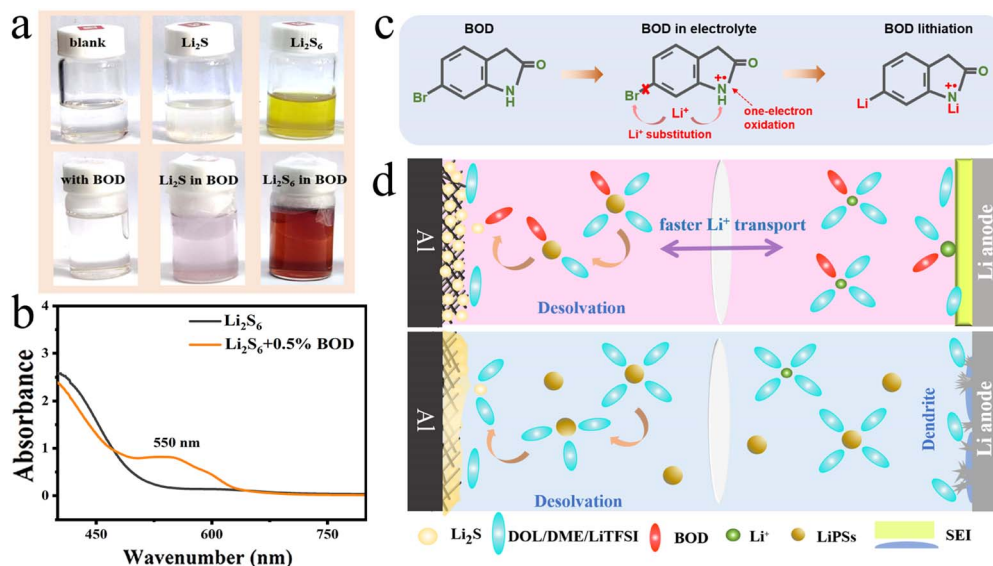


Fig. 1 Reversible evolution of the BOD additive under Li–S chemistry. (a) Digital photographs of a traditional DOL/DME-based electrolyte (blank) with Li₂S and Li₂S₆ species before and after the addition of the BOD additive. (b) UV-vis spectra of Li₂S₆-based electrolytes with/without BOD. (c) Multiple electrochemical lithiation steps of the BOD: original, solvated and lithiated states. (d) Schematic diagram of BOD in the solvation structure and its impact on Li deposition and S conversions.

to the characteristic signal of the BOD molecule, and two peaks at ~256 and 295 nm ascribed to LiPSs shifted after the BOD addition. Thus, the BOD additive changed the solvation structures of the traditional Li–S electrolyte (1 wt% LiNO₃ and 1.0 M LiTFSI in DOL/DME with v/v = 1 : 1).

It has been reported that, in mechanochemical synthesis, indole compounds tend to undergo directional electron movements under the action of an electric field, resulting in the removal of single electrons and the formation of electron-deficient intermediates.²⁹ Additionally, the cyclic voltammetry (CV) tests reconfirmed that BOD undergoes redox reactions when added to Li–S electrolyte (Fig. S4†). Single electron oxidation is an efficient approach to indole compound conversion. Additionally, indole homologs can form cation– π interactions with Li⁺, which regulate its transport through the electron-rich conjugated structure.^{34–36} In the case of the additive, BOD undergoes partial deprotonation and combines with Li⁺ and anions in solution to stabilize its structure during charging and discharging (Fig. 1c). This is because the cyclic amide group with p– π conjugation can easily dehydrogenate in the presence of organic electrolytes with lithium salts, forming more stable Li–N bonds.^{31,33} In Li–S chemistry, externally suspended Li atoms can act as cationic centers that bind with TFSI[–] and/or polysulfide anions (PS[–]). Moreover, halogen bromide ions act as a sacrificial agent,³⁷ easily detaching from BOD and reacting with metallic Li to form a stable solid electrolyte interphase (SEI) film at the anode side. Thus, BOD as an electrolyte mediator, can regulate sulfur redox reactions at the cathode to form a more stable Li anode in the Li–S battery system (Fig. 1d).

LiPS conversions mediated by BOD

The influence of BOD on sulfur reduction reactions was examined in terms of the Li₂S deposition behaviors (Fig. 2a–c). As

shown in the current–time (*i*–*t*) curves for the Li₂S deposition, the response time (*t*_m) for reaching the peak current (*i*_m) depended on the amount of BOD added, where a higher BOD concentration induced faster Li₂S deposition (blank, *t*_m = 4200 s; 0.5 wt% BOD, *t*_m = 3178 s; 5 wt% BOD, *t*_m = 1190 s). Moreover, we calculated the Li₂S deposition capacity according to Faraday's law. The best performance was achieved by the 0.5 wt% BOD cell that delivered a capacity of 737.91 mA h g^{–1}, which is much higher than that of the 5 wt% BOD (410.84 mA h g^{–1}) and control cells (129.93 mA h g^{–1}). Thus, the BOD additive can mediate the LiPS to Li₂S conversion. To clarify this phenomenon, a dimensionless analysis of *i*–*t* curves was performed based on both the Scharifker–Hills (SH)^{38,39} and Bewick–Fleischman–Thirsk (BFT) models⁴⁰ (Fig. 1d). The nucleation rates of two-dimensional progressive nucleation (2DP) and instantaneous deposition (2DI) are controlled by the adatom crystal phase, whereas the nucleation rates of 3D progressive nucleation (3DP) and 3D instantaneous deposition (3DI) are mainly determined by volume diffusion (Fig. 2d).

As shown in Fig. 2e, on the addition of 0.5 wt% BOD to the electrolyte, the Li₂S deposition mode changed from 2DP to 2DI. As the BOD percentage was increased to 5 wt%, the deposition switched to the 3DI mode. This behavior can be attributed to the fact that BOD dissolves Li₂S, resulting in proper solubility of Li₂S, which regulates the nucleation and growth of polysulfide particles in the solution.⁴¹ The SEM images show large spherical Li₂S particles densely deposited in the control cell (Fig. 2f), which likely contributed to low electrochemical conversion activity and uneven electron conduction. The spherical Li₂S particles of the 0.5 wt% BOD battery were uniformly deposited with a diameter of 1.8 μ m (Fig. 2g), and are likely to promote channels for ion/electron transfer and improve the electrochemical conversion activity. As the BOD additive content was

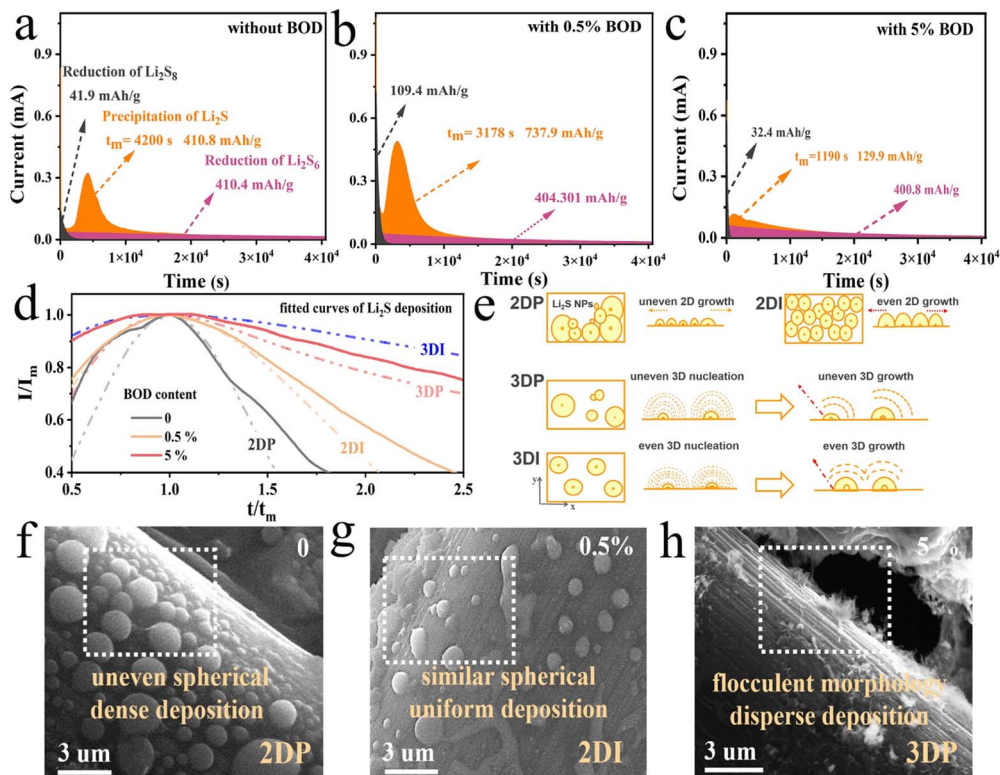


Fig. 2 Deposition pathway and morphology of sulfur species at the cathode with the 0.5% BOD additive. (a–c) Chronoamperograms of Li_2S precipitation at 2.10 V in electrolyte without BOD, 0.5 wt% BOD, and 5 wt% BOD. The parameter i_m represents the peak current and t_m is the deposition time to reach the peak current. (d) Comparison of transient current–time response curves (solid line) with classical 2DP, 2DI, 3DP, and 3DI nucleation models (dashed line). (e) Schematic illustration of 3DP/3DI and 2DP/2DI Li_2S depositions where x – y is parallel to the substrate and y – z is vertical to the substrate. (f–h) SEM images of Li_2S deposition in electrolytes with 0.5 wt% BOD and 5 wt% BOD, respectively, as well as without BOD. The tests were performed on carbon cloth frameworks.

increased to 5 wt%, the Li_2S deposition exhibited a flocculent morphology with a loose mass and electrical contacts where the chemical reaction dominated rather than the electrochemical reactions (Fig. 2h). Hence, the optimal amount of BOD induced rapid nucleation and growth of Li_2S , which is likely to improve the deposition capacity and enhance the Li–S battery kinetics.

Kinetic evaluations for sulfur redox reactions

To quantify the improvement in kinetics, we calculated the Li^+ diffusion coefficient (D_{Li^+}) of the 0.5 wt% BOD cell by performing CV tests over a scanning range of 0.1–0.3 mV s^{-1} . As shown in Fig. 3a and S5a,† the 0.5 wt% BOD battery exhibited much higher anodic (A and B) and cathodic (C and D) current peaks than those of the control sample. By fitting the peak current (I_p) and the square root of the scanning rate ($\nu^{0.5}$), a linear functional relationship was found for both samples, indicative of a typical ion diffusion-controlled reaction (Fig. 3b and S5b†). According to the Randles–Sevcik equation, D_{Li^+} of the 0.5 wt% BOD cell (A, 4.3×10^{-8} ; B, 6.4×10^{-8} ; C, 0.5×10^{-8} ; D, $2.8 \times 10^{-8} \text{ cm}^2 \text{ s}^{-1}$) was ~ 2 times as high as that of the blank sample (A, 2.8×10^{-8} ; B, 3.2×10^{-8} ; C, 1.6×10^{-8} ; D, $1.1 \times 10^{-8} \text{ cm}^2 \text{ s}^{-1}$), suggesting excellent Li^+ transport kinetics.

Electrochemical impedance spectroscopy (EIS) measurements were conducted under the operating conditions to

characterize the electron/ion transport behaviors in the liquid electrolytes, bulk electrodes, and between these phases. As shown in Fig. 3c, the interface resistance (R_{int}) of the 0.5 wt% BOD battery increased from 2.49 to 9.26 Ω after the first 150 cycles and then decreased to 1.88 Ω by 200 cycles, whereas the charge transfer resistance (R_{ct}) continuously decreased from 45.12 to 43.52 Ω . These results indicate the gradual formation of a stable solid electrolyte interphase (SEI) and rapid mass transfer performance in this modified electrolyte system.

As mentioned above, *operando* detection technology can provide more information on intermediate states of the working cell. The potentiostatic intermittent titration technique (PITT) and galvanostatic intermittent titration technique (GITT) were used to study the *in situ* sulfur conversion processes and electrochemical polarization characteristics. Fig. 3d shows the PITT plots of the 0.5 wt% BOD cell in the initial discharge cycle, where the first region (2.40–2.10 V) corresponds to long-chain to short-chain LiPS conversion and the second region (2.10–1.60 V) is assigned to short-chain LiPS to $\text{Li}_2\text{S}_2/\text{Li}_2\text{S}$ conversion. The response current of the 0.5 wt% BOD cell was consistently greater than that of the control cell and it achieved higher deposition voltages. The Li_2S_6 symmetric cell tests confirmed that BOD could accelerate the liquid–liquid conversion of LiPS (Fig. S6†). As for the GITT tests (Fig. 3e), the voltage at each galvanostatic discharge and relaxation pulse was plotted as

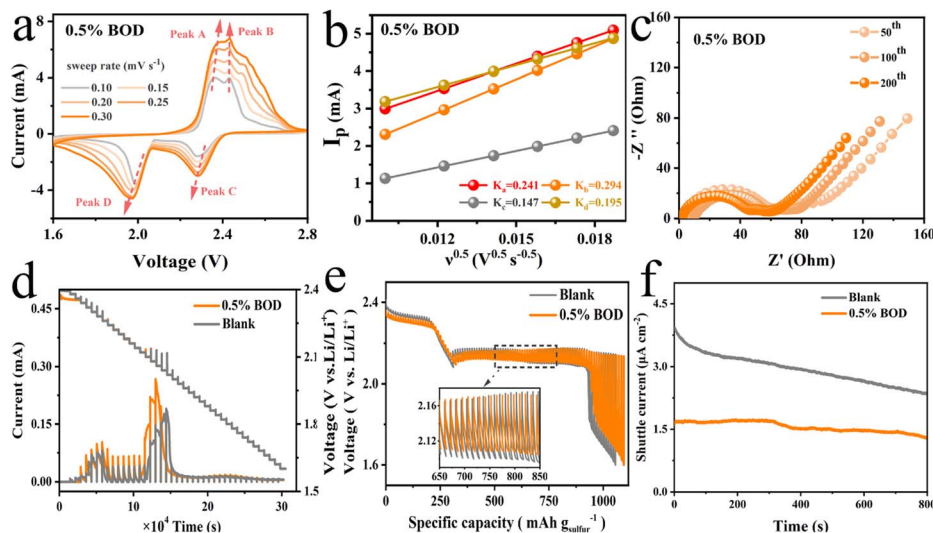


Fig. 3 Kinetic evaluations of 0.5 wt% BOD for sulfur redox reactions. (a) Cyclic voltammograms tests of the 0.5 wt% BOD battery at different scanning rates. (b) Li^+ diffusion coefficients of the 0.5 wt% battery determined by fitting the scanning rate-dependent peak currents. (c) Nyquist plots of the 0.5 wt% BOD battery after 50, 100, and 200 cycles. (d–f) PITT, GITT, and shuttle current tests of batteries with/without 0.5 wt% BOD.

a function of discharge capacity. These results showed that the 0.5 wt% BOD cell had a 45 mV voltage gap between the reduction voltage and corresponding open-circuit voltage, which was much smaller than that of the blank sample (77 mV). Thus, 0.5 wt% BOD can reduce the iR drop and electrochemical polarization, to facilitate Li^+ /electron supplementation and improve sulfur redox reactions. The internal resistance was calculated based on the GITT which showed that BOD mainly promotes sulfur conversion kinetics in liquid–solid reactions (Fig. S7†). Additionally, the LiPS shuttle current was markedly suppressed to $\sim 1.5 \times 10^{-3} \text{ mA cm}^{-2}$ in the presence of 0.5% BOD, which is half the value of the control cell ($\sim 3.0 \times 10^{-3} \text{ mA cm}^{-2}$) (Fig. 3f). These results suggest that BOD can effectively suppress the shuttle effect.

Li plating/stripping behaviors

Single electron oxidation of BOD induces its combination with Li^+ /LiPSs and thus alters the solvation structure. To study the transport behavior of Li^+ and/or LiPSs and the flux of these species at the anode, a series of tests were conducted on Li||Li symmetrical cells with and without the 0.5 wt% BOD additive. As shown in Fig. 4a and b, there were clear differences in SEM images of the Li surface after 200 successive plating/stripping cycles. The blank sample had uneven nanofiber Li dendrites with large amounts of irreversibly inactivated Li whereas the 0.5 wt% BOD sample was flat without any cracks and a few inactive Li particles.

Moreover, in the former cell, the Li was black while the latter retained its original metallic luster (Fig. 4a and b insets). Thus, 0.5 wt% BOD promotes good reversibility for metallic Li. As a result, even under harsh conditions (-20°C), the metallic Li in 0.5 wt% BOD remained flat without any dendrite formation (Fig. S8†). Electrochemical impedance spectroscopy (EIS) and galvanostatic cycling performance were used to monitor the

interfacial evolution. Fig. 4c and S9† show Nyquist plots of the Li||Li symmetrical cells of the 0.5 wt% BOD sample at a current density of 1 mA cm^{-2} and a capacity of 1 mA h cm^{-2} . The 0.5 wt% BOD sample showed a characteristic SEI signal after cycling for 8 h, and then the impedance decreased and quickly stabilized. In contrast, the blank sample underwent notable changes that could be attributed to the continuous formation and rupture of the SEI on the Li anode. Regarding the galvanostatic cycling performance (Fig. 4d), the polarization voltage of the 0.5 wt% BOD cell increased from 48 mV at 0.2 mA cm^{-2} to 203.7 mV at 5 mA cm^{-2} . Notably, these values are much smaller and more stable than those of the blank sample (150.7 mV at 0.2 mA cm^{-2} to 406.9 mV at 5 mA cm^{-2}). The galvanostatic cycling performance of the Li||Li symmetrical cells in Fig. 4e indicated that the BOD stabilized the Li anode for more than 450 h with a low voltage hysteresis of $\sim 40 \text{ mV}$. Conversely, the blank sample maintained stable cycling for less than 300 h and rapidly deteriorated with a voltage hysteresis of $\sim 130 \text{ mV}$.

Remarkably, as shown in Fig. S10,† we directly immersed Li sheets in an electrolyte containing 0.5 wt% BOD and found that the color turned yellow. This change indicates a chemical reaction between BOD and metallic Li, which is consistent with the aforementioned Li intercalation mechanisms (Fig. 1c). The repairing effect of BOD on the Li anode can be verified by studying its surface compositions and chemical states. Fig. 4f shows high-resolution Br 3d X-ray photoelectron spectroscopy (XPS) measurements of Li anodes after the 0.5 wt% BOD cell had operated for 0 and 200 cycles. Both samples featured LiBr signals (at 68.9 eV after 200 cycles and 68.4 eV in the initial state), which can be attributed to the chemical reaction of BOD and metallic Li, and helps to form an inorganic SEI layer on the anode.⁴² Moreover, the Li 1s XPS results revealed the presence of LiF (53.2 eV) (Fig. S11 and S12†). The LiF/LiBr rich SEI can improve the stability and reversibility of the Li anode, which is in agreement with previous reports.^{43–45}

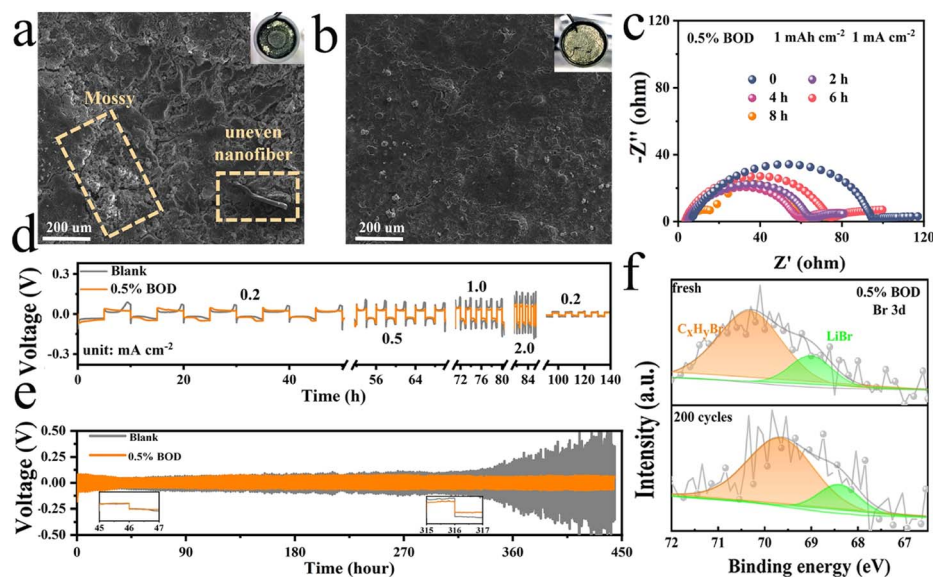


Fig. 4 (a) Li plating/stripping behaviors in Li-S cells with the BOD additive. (a and b) SEM images of metallic Li after 200 successive cycles before and after the addition of 0.5 wt% BOD. Insets show corresponding optical photographs. (c) EIS of 0.5 wt% BOD cells after Li plating/stripping for 0, 2, 4, 6, and 8 h at a current density of 1 mA cm⁻² and a capacity density of 1 mA h cm⁻². (d) Li plating/stripping curves of 0.5 wt% BOD cells at current densities in the range of 0.2–2.0 mA cm⁻². (e) Long-term Li plating/stripping profiles of 0.5 wt% BOD cells at a current density of 1 mA cm⁻² and capacity density of 1 mA h cm⁻². (f) High-resolution Br 3d XPS spectra of the metallic Li anode in 0.5 wt% BOD-based Li-S batteries after 0 and 200 cycles.

Dynamic solvation/de-solvation behaviors

To further analyze the BOD-dominated solvation structure, *ex/in situ* Raman spectroscopy, and Fourier transform infrared spectroscopy (FT-IR) were conducted on samples based on

a typical Li-S electrolyte. As shown in Fig. 5a, addition of 0.5 wt% BOD altered the Raman signals. The peak at 740 cm⁻¹, assigned to the stretching vibration of S–N–S in TFSI⁻,^{46,47} weakened and a new peak emerged at 723 cm⁻¹. At the same time, the Raman signals of DME underwent a considerable

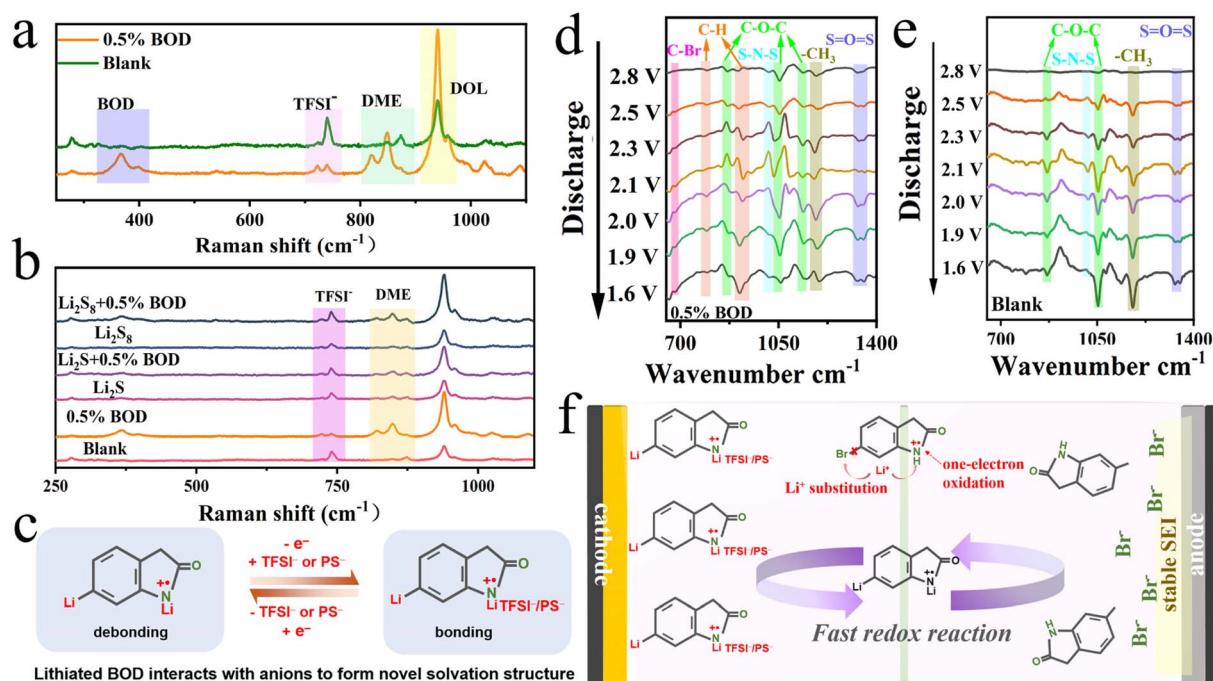


Fig. 5 BOD mediated solvation and de-solvation behaviors with dynamic evolution. (a) Raman spectra of traditional Li-S electrolyte with and without 0.5 wt% BOD. Raman spectra of (b) 0.02 M of Li₂S and Li₂S₈ solutions with 0.5 wt% BOD. (c) Reversible association/dissociation of lithiated BOD with PS⁻/TFSI⁻ anions. (d and e) *In situ* FT-IR measurements of the cells with and without 0.5 wt% BOD at different discharge depths. (f) Schematic diagram of BOD for the formation of a new solvation structure and its effects on Li deposition and sulfur conversion.

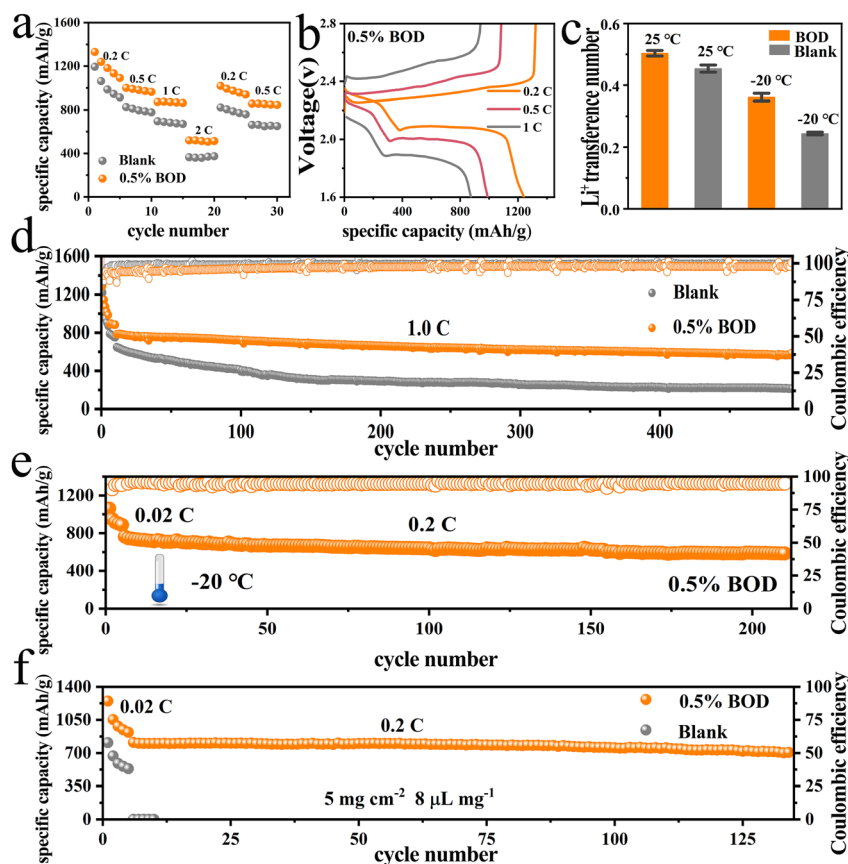


Fig. 6 Electrochemical performances of Li-S batteries with 0.5 wt% BOD. (a) Rate capability and (b) GCD curves of the 0.5 wt% BOD cell at the rate of 0.2 to 2C. (c) Li^+ migration numbers of the electrolyte with and without BOD at temperatures of 25 and -20°C . Long-term cycling performances of cells (d) at a rate of 1C and (e) under a high sulfur loading of 5 mg cm^{-2} with an E/S ratio of $8\text{ }\mu\text{L mg}^{-1}$. (f) -20°C cycling properties of the 0.5 wt% BOD cell at 0.2C.

blue-shift and peak intensity enhancement after the addition of 0.5 wt% BOD. The signal of the free DME solvent⁴⁸ shifted from 847 to 823 cm^{-1} , whereas the signal of Li^+ coordinated DME⁴⁹ shifted from 873 to 849 cm^{-1} . The emergence of new peaks and the blue-shift of the DME signals could be attributed to the BOD and TFSI⁻ interactions, which affected the solvation structures.^{50–52} Raman measurements were also performed in the presence of various LiPSs (Fig. 5b, S13 and S14[†]). The stretching vibration peaks of the S-S bond (534 cm^{-1}) from LiPSs and S-N-S bonds (740 cm^{-1}) from TFSI⁻ were enhanced, whereas the binding affinity of TFSI⁻ with BOD, as evaluated from the peak at $\sim 723\text{ cm}^{-1}$, was weakened, indicating that BOD participated not only in the solvation of LiPSs but also in the dissociation of LiTFSI (Fig. 5c). Notably, the BOD-involved electrolyte also accelerated sulfur conversion, as confirmed by the peak intensity decrease of sulfur signals as the BOD content increased (Fig. S15[†]). Moreover, we further detected ion cluster signals at 745 cm^{-1} , *i.e.*, contact-ion-pairs (CIPs) between TFSI⁻ anions and Li^+ ,⁵³ in the discharge process.

As shown in Fig. 5d, *in situ* FT-IR spectroscopy was performed to monitor changes in organic functional groups of the solvation structures during the discharge of the 0.5 wt% BOD cell from 2.8 to 1.6 V . In the initial stage (2.8 – 2.4 V),

characteristic signals of DOL, DME, TFSI⁻, and BOD were detected, where the peaks at 1184 cm^{-1} and $868/1054/1135\text{ cm}^{-1}$ are vibrational signals of $-\text{CH}_3$ and $\text{C}-\text{O}-\text{C}$ from DOL/DME; the peaks at 1018 and 1355 cm^{-1} belong to the ν_{as} vibrations of S-N-S and $\text{S}=\text{O}=\text{S}$ from TFSI⁻; and the peaks at 682 and $795/920\text{ cm}^{-1}$ are assigned to the out-of-plane bending vibrations of C-Br and benzene ring C-H groups of BOD, respectively.^{54–59} In the subsequent stage (2.4 – 2.0 V), the solvation structure changed as the polysulfide chain length decreased. Hence, a red shift (from 1054 to 1040 cm^{-1}) and peak intensity increase of C-O-C vibrations were found in DOL/DME solvents, indicating an increase of free solvent molecules. This result can be attributed to competitive coordination with Li salts (*e.g.*, LiPSs and LiTFSI) between BOD and solvent molecules. The weakened C-H signal (795 cm^{-1}) and enhanced C-Br signal suggest that BOD has multiple binding sites to bond with Li salts, as demonstrated by the peak intensity increase of the $\text{S}=\text{O}=\text{S}$ signal (from TFSI⁻), which arises from the dissociation of LiTFSI from DOL/DME solvents and association with BOD. In the last stage (2.0 to 1.6 V), soluble LiPSs were converted to solid $\text{Li}_2\text{S}_2/\text{Li}_2\text{S}$, and free solvent was released in large quantities. Therefore, the C-H bending vibration and C-O-C stretching vibration of DOL/DME were significantly enhanced. Conversely,

the blank cell showed no obvious peak shifts except for some intensity changes owing to Li-S reactions (Fig. 5e). These findings demonstrated that the addition of 0.5 wt% BOD can dynamically tailor solvation structures in bulk electrolytes and mediate sulfur conversion.

Fig. 5f shows a schematic illustration of the mechanism by which 0.5 wt% BOD influences the Li-S chemistry. In the electrolyte, BOD undergoes an initial lithiation process and induces reconstruction of solvation structures, resulting in rapid movements of Li^+ ions. At the anode side, pretreatment with highly reactive BOD established a stable and uniform SEI on the Li anode. At the cathode, solvated BOD is capable of accelerating Li_2S formation and mediating its nucleation and growth from 2DI to 3DP morphologies, thereby enhancing sulfur utilization. Consequently, the 0.5 wt% BOD cell exhibited improved sulfur conversion kinetics and high sulfur utilization while maintaining a stable Li anode.

Electrochemical performances

We further evaluated the electrochemical performance of 0.5 wt% BOD batteries by comparing the constant current charge/discharge (GCD) measurements of the second cycle. The capacities of cells with various amounts of BOD are shown in Fig. 6a and S16†. The 0.5 wt% BOD cell delivered a high discharge capacity of 1330, 1000, 872, and 519 mA h g^{-1} at 0.2, 0.5, 1, and 2 C, respectively. This performance was much better than that of other cells, namely: 0.1 wt% BOD (1349, 946, 837, and 400 mA h g^{-1}); 1 wt% BOD (922, 612, 519, and 390 mA h g^{-1}); and the control (1193, 826, 695, and 364 mA h g^{-1}). When the current rate of the 0.5 wt% BOD cell was recovered to 0.2 C, a highly reversible discharge capacity of 1018 mA h g^{-1} was achieved with a long and flat discharge plateau (Fig. 6b and S17†).

Thus, the addition of 0.5 wt% BOD provided the optimal performance and markedly enhanced battery performance. An excess of the BOD additive is likely to increase uncoordinated BOD and hinder Li^+ transport in the electrolyte. Insufficient additives may lead to incomplete SEI layers at the Li anode. The average Li^+ migration numbers of BOD at 25 °C and -20 °C were 0.51 and 0.38, respectively, which were better than those of the blank cell (0.4 and 0.24) (Fig. 6c). By measuring the migration number of Li^+ at different temperatures, it was demonstrated that the solvation structure formed by BOD in the electrolyte has good Li^+ transport characteristics (Fig. S18†). The cycling performances of the 0.5 wt% BOD cell were measured at a high current rate (Fig. 6d), high sulfur loading, low E/S ratio (Fig. 6e), and low temperature (Fig. 6f). After initial activation, the cell exhibited a high initial discharge capacity of 783 mA h g^{-1} at 1 C and maintained a capacity of 576 mA h g^{-1} after 500 cycles with a mean decay rate of 0.05% per cycle and a coulombic efficiency of 97.875%. When the cell operated at a sulfur loading of 5 mg cm^{-2} (cathode thickness: $\sim 220 \mu\text{m}$, Fig. S19†) and E/S ratio of 8 $\mu\text{L mg}^{-1}$, a high discharge capacity of 811 mA h g^{-1} was obtained at 0.2 C and maintained at 730 mA h g^{-1} after 120 cycles. Hence, the 0.5 wt% BOD cell performed better than the control cell in terms of capacity and stability. Additionally, owing to the

involvement of BOD in the solvation structure, the 0.5 wt% BOD cell could operate stably at a low temperature of -20 °C, delivering a discharge capacity of 590 mA h g^{-1} at 0.2 C with a decay rate of 0.11% per cycle.

Conclusions

In summary, we have successfully introduced an electrolyte additive BOD into Li-S batteries to accelerate Li^+ transfer kinetics and promote interfacial compatibility. The BOD additive undergoes single electron oxidation under an electric field and has cation- π interactions with Li^+ . Owing to the electron-rich conjugated structure, the BOD-modified electrolyte can regulate the solvation structure of Li^+ and LiPS, mediate their transport in the electrolyte, increase uniform Li-ion flux, and tailor interfacial chemistry at the cathode and anode electrodes. The Li_2S deposition mode on the cathode changes with increased addition of BOD and, when 0.5 wt% BOD is added, the Li_2S deposition mode switches to 2DI with high sulfur utilization. The Li anode remains stable at various current densities and temperatures owing to the formation of a robust SEI comprising LiF/LiBr. As a result, the 0.5 wt% BOD batteries exhibited excellent long-term cycling performance at low temperatures (-20 °C) and under lean electrolyte/high loading conditions (E/S ratio of 8 $\mu\text{L mg}^{-1}$ and sulfur loading of 5 mg cm^{-2}). This work proposes a simple strategy to improve Li-S battery performance based on the use of a trace electrolyte additive. These findings will broaden our understanding of Li-S electrolytes, paving the way for highly stable practical Li-S batteries that are capable of operating under extreme conditions, such as high energy densities, lean electrolytes, and low temperatures.

Author contributions

Jinxuan Zou: conceptualization, methodology, validation, investigation, writing – original draft, writing – review & editing, visualization. Dong Cai: writing – review & editing. Pengxuan He: investigation. Yufang Zhang: investigation. Ying He: investigation. Yangyang Dong: investigation. Kuikui Xiao: investigation. Xuemei Zhou: investigation. Huagui Nie: investigation. Shuo Yang: writing – review & editing. Zhi Yang: supervision, writing – review & editing.

Conflicts of interest

There are no conflicts to declare.

Acknowledgements

The authors greatly acknowledge the support of the Natural Science Foundation of Zhejiang Province (Grant No. LQ22B030003), National Natural Science Foundation of China (Grant No. 22309136, 22109119 and 51972238), Graduate Scientific Research Foundation of Wenzhou University (Grant No. 3162023003039) and Xinmiao Foundation of Zhejiang Province (Grant No. 2023R451052).

Notes and references

- 1 N. Nakamura, S. Ahn, T. Momma and T. Osaka, *J. Power Sources*, 2023, **558**, 232566.
- 2 F. Liu, C. Zong, L. He, Z. Li, B. Hong, M. Wang, Z. Zhang, Y. Lai and J. Li, *Chem. Eng. J.*, 2022, **443**, 136489.
- 3 H. Sul, A. Bhargava and A. Manthiram, *Adv. Energy Mater.*, 2022, **12**, 2200680.
- 4 Z. Pan, D. J. L. Brett, G. He and I. P. Parkin, *Adv. Energy Mater.*, 2022, **12**, 2103483.
- 5 M. Zhao, B.-Q. Li, H.-J. Peng, H. Yuan, J.-Y. Wei and J.-Q. Huang, *Angew. Chem., Int. Ed.*, 2020, **59**, 12636–12652.
- 6 B. Yang, D. Guo, P. Lin, L. Zhou, J. Li, G. Fang, J. Wang, H. Jin, X. a. Chen and S. Wang, *Angew. Chem., Int. Ed.*, 2022, **61**, e202204327.
- 7 Z. Wei, Y. Ren, J. Sokolowski, X. Zhu and G. Wu, *InfoMat*, 2020, **2**, 483–508.
- 8 Z. Ning, G. Li, D. L. R. Melvin, Y. Chen, J. Bu, D. Spencer-Jolly, J. Liu, B. Hu, X. Gao, J. Perera, C. Gong, S. D. Pu, S. Zhang, B. Liu, G. O. Hartley, A. J. Bodey, R. I. Todd, P. S. Grant, D. E. J. Armstrong, T. J. Marrow, C. W. Monroe and P. G. Bruce, *Nature*, 2023, **618**, 287–293.
- 9 T. Tao, S. Lu, Y. Fan, W. Lei, S. Huang and Y. Chen, *Adv. Mater.*, 2017, **29**, 1700542.
- 10 S. Wang, B. Lu, D. Cheng, Z. Wu, S. Feng, M. Zhang, W. Li, Q. Miao, M. Patel, J. Feng, E. Hopkins, J. Zhou, S. Parab, B. Bhamwala, B. Liaw, Y. S. Meng and P. Liu, *J. Am. Chem. Soc.*, 2023, **145**, 9624–9633.
- 11 T. Wang, J. He, X.-B. Cheng, J. Zhu, B. Lu and Y. Wu, *ACS Energy Lett.*, 2023, **8**, 116–150.
- 12 L.-P. Hou, N. Yao, J. Xie, P. Shi, S.-Y. Sun, C.-B. Jin, C.-M. Chen, Q.-B. Liu, B.-Q. Li, X.-Q. Zhang and Q. Zhang, *Angew. Chem., Int. Ed.*, 2022, **61**, e202201406.
- 13 Y. Liu, Y. Elias, J. Meng, D. Aurbach, R. Zou, D. Xia and Q. Pang, *Joule*, 2021, **5**, 2323–2364.
- 14 Z. Shi, Z. Tian, D. Guo, Y. Wang, Z. Bayhan, A. S. Alzahrani and H. N. Alshareef, *ACS Energy Lett.*, 2023, **8**, 3054–3080.
- 15 G. Liu, Q. Sun, Q. Li, J. Zhang and J. Ming, *Energy Fuels*, 2021, **35**, 10405–10427.
- 16 S. Tan, Z. Shadike, J. Li, X. Wang, Y. Yang, R. Lin, A. Cresce, J. Hu, A. Hunt, I. Waluyo, L. Ma, F. Monaco, P. Cloetens, J. Xiao, Y. Liu, X.-Q. Yang, K. Xu and E. Hu, *Nat. Energy*, 2022, **7**, 484–494.
- 17 D.-Y. Wang, Y. Si, W. Guo and Y. Fu, *Nat. Commun.*, 2021, **12**, 3220.
- 18 Z. Shen, W. Zhang, S. Mao, S. Li, X. Wang and Y. Lu, *ACS Energy Lett.*, 2021, **6**, 2673–2681.
- 19 J. Jung, H. Chu, I. Kim, D. H. Lee, G. Doo, H. Kwon, W. Jo, S. Kim, H. Cho and H.-T. Kim, *Adv. Sci.*, 2023, **10**, 2301006.
- 20 X.-Y. Li, S. Feng, C.-X. Zhao, Q. Cheng, Z.-X. Chen, S.-Y. Sun, X. Chen, X.-Q. Zhang, B.-Q. Li, J.-Q. Huang and Q. Zhang, *J. Am. Chem. Soc.*, 2022, **144**, 14638–14646.
- 21 X. Yao, J. Wang, S. Lin, C. Tao, X. Zhang, W. Wang, C. Zhao, L. Wang, J. L. Bao, Y. Wang and T. Liu, *Adv. Energy Mater.*, 2023, **13**, 2203233.
- 22 X. Wu, Q. Zhang, G. Tang, Y. Cao, H. Yang, H. Li and X. Ai, *Small*, 2022, **18**, 2106144.
- 23 S. Zhou, S. Yang, X. Ding, Y. Lai, H. Nie, Y. Zhang, D. Chan, H. Duan, S. Huang and Z. Yang, *ACS Nano*, 2020, **14**, 7538–7551.
- 24 S. Zhou, S. Yang, D. Cai, C. Liang, S. Yu, Y. Hu, H. Nie and Z. Yang, *Adv. Sci.*, 2022, **9**, 2104205.
- 25 T. Li, D. Cai, S. Yang, Y. Dong, S. Yu, C. Liang, X. Zhou, Y. Ge, K. Xiao, H. Nie and Z. Yang, *Adv. Mater.*, 2022, **34**, 2207074.
- 26 S.-Y. Jiang, J. Shi, W. Wang, Y.-Z. Sun, W. Wu, J.-R. Song, X. Yang, G.-F. Hao, W.-D. Pan and H. Ren, *ACS Catal.*, 2023, **13**, 3085–3092.
- 27 C. Song, K. Liu, X. Jiang, X. Dong, Y. Weng, C.-W. Chiang and A. Lei, *Angew. Chem., Int. Ed.*, 2020, **59**, 7193–7197.
- 28 J. Shi, R.-A. Wang, W. Wu, J.-R. Song, Q. Chi, W.-D. Pan and H. Ren, *Org. Lett.*, 2022, **24**, 3358–3362.
- 29 W. Wei, G. Chang, Y. Xu and L. Yang, *J. Mater. Chem. A*, 2018, **6**, 18794–18798.
- 30 G. Zhao and H. Zhu, *Adv. Mater.*, 2020, **32**, 1905756.
- 31 K. S. Ryu and K. M. Kim, *J. Appl. Electrochem.*, 2008, **38**, 477–482.
- 32 B. B. Berkes, A. S. Bandarenka and G. Inzelt, *J. Phys. Chem. C*, 2015, **119**, 1996–2003.
- 33 R. Chulliyote, H. Hareendrakrishnakumar, M. Raja, J. M. Gladis and A. M. Stephan, *Sustainable Energy Fuels*, 2017, **1**, 1774–1781.
- 34 Y. Wang, X.-J. Zhao, X. Wu, L. Zhang, G. Li and Y. He, *ChemElectroChem*, 2022, **9**, e202200378.
- 35 W. Sun, C. Zhou, Y. Fan, Y. He, H. Zhang, Z. Quan, H. Kong, F. Fu, J. Qin, Y. Shen and H. Chen, *Angew. Chem., Int. Ed.*, 2023, **62**, e202300158.
- 36 J.-Y. Wang, Y.-M. Su, F. Yin, Y. Bao, X. Zhang, Y.-M. Xu and X.-S. Wang, *Chem. Commun.*, 2014, **50**, 4108–4111.
- 37 H. Chu, H. Noh, Y.-J. Kim, S. Yuk, J.-H. Lee, J. Lee, H. Kwack, Y. Kim, D.-K. Yang and H.-T. Kim, *Nat. Commun.*, 2019, **10**, 188.
- 38 B. Scharifker and G. Hills, *Electrochim. Acta*, 1983, **28**, 879–889.
- 39 M. E. Hyde and R. G. Compton, *J. Electroanal. Chem.*, 2003, **549**, 1–12.
- 40 A. Bewick, M. Fleischmann and H. Thirsk, *Trans. Faraday Soc.*, 1962, **58**, 2200–2216.
- 41 H. Pan, J. Chen, R. Cao, V. Murugesan, N. N. Rajput, K. S. Han, K. Persson, L. Estevez, M. H. Engelhard and J.-G. Zhang, *Nat. Energy*, 2017, **2**, 813–820.
- 42 S. Qi, J. He, J. Liu, H. Wang, M. Wu, F. Li, D. Wu, X. Li and J. Ma, *Adv. Funct. Mater.*, 2021, **31**, 2009013.
- 43 S. Zhou, Y. Zhu, H. Hu, C. Li, J. Jiang, J. Huang and B. Zhang, *J. Mater. Chem. A*, 2023, **11**, 5636–5644.
- 44 W. Yu, Z. Yu, Y. Cui and Z. Bao, *ACS Energy Lett.*, 2022, **7**, 3270–3275.
- 45 P. Liu, H. Su, Y. Liu, Y. Zhong, C. Xian, Y. Zhang, X. Wang, X. Xia and J. Tu, *Small Struct.*, 2022, **3**, 2200010.
- 46 R. Meng, X. He, S. J. H. Ong, C. Cui, S. Song, P. Paoprasert, Q. Pang, Z. J. Xu and X. Liang, *Angew. Chem., Int. Ed.*, 2023, e202309046.

- 47 J. Fu, X. Ji, J. Chen, L. Chen, X. Fan, D. Mu and C. Wang, *Angew. Chem., Int. Ed.*, 2020, **59**, 22194–22201.
- 48 Q. Sun, Z. Cao, Z. Ma, J. Zhang, W. Wahyudi, G. Liu, H. Cheng, T. Cai, E. Xie, L. Cavallo, Q. Li and J. Ming, *Adv. Funct. Mater.*, 2023, **33**, 2210292.
- 49 Z. Huang, J.-C. Lai, X. Kong, I. Rajkovic, X. Xiao, H. Celik, H. Yan, H. Gong, P. E. Rudnicki, Y. Lin, Y. Ye, Y. Li, Y. Chen, X. Gao, Y. Jiang, S. Choudhury, J. Qin, J. B. H. Tok, Y. Cui and Z. Bao, *Matter*, 2023, **6**, 445–459.
- 50 L. Dong, Y. Liu, K. Wen, D. Chen, D. Rao, J. Liu, B. Yuan, Y. Dong, Z. Wu and Y. Liang, *Adv. Sci.*, 2022, **9**, 2104699.
- 51 G. Park, K. Lee, D.-J. Yoo and J. W. Choi, *ACS Energy Lett.*, 2022, **7**, 4274–4281.
- 52 D.-Y. Wang, W. Wang, F. Li, X. Li, W. Guo and Y. Fu, *J. Energy Chem.*, 2022, **71**, 572–579.
- 53 H. Zhang, Z. Zeng, F. Ma, Q. Wu, X. Wang, S. Cheng and J. Xie, *Angew. Chem., Int. Ed.*, 2023, **62**, e202300771.
- 54 D. Aurbach, E. Pollak, R. Elazari, G. Salitra, C. S. Kelley and J. Affinito, *J. Electrochem. Soc.*, 2009, **156**, A694.
- 55 L. Lodovico, A. Varzi and S. Passerini, *J. Electrochem. Soc.*, 2017, **164**, A1812.
- 56 W. Kam, C.-W. Liew, J. Lim and S. Ramesh, *Ionics*, 2014, **20**, 665–674.
- 57 Q. Liu, F. Wu, D. Mu and B. Wu, *Chin. Phys. B*, 2020, **29**, 048202.
- 58 B. N. Olana, S. D. Lin and B.-J. Hwang, *Electrochim. Acta*, 2022, **416**, 140266.
- 59 J. Yu, X. Lin, J. Liu, J. T. T. Yu, M. J. Robson, G. Zhou, H. M. Law, H. Wang, B. Z. Tang and F. Ciucci, *Adv. Energy Mater.*, 2022, **12**, 2102932.